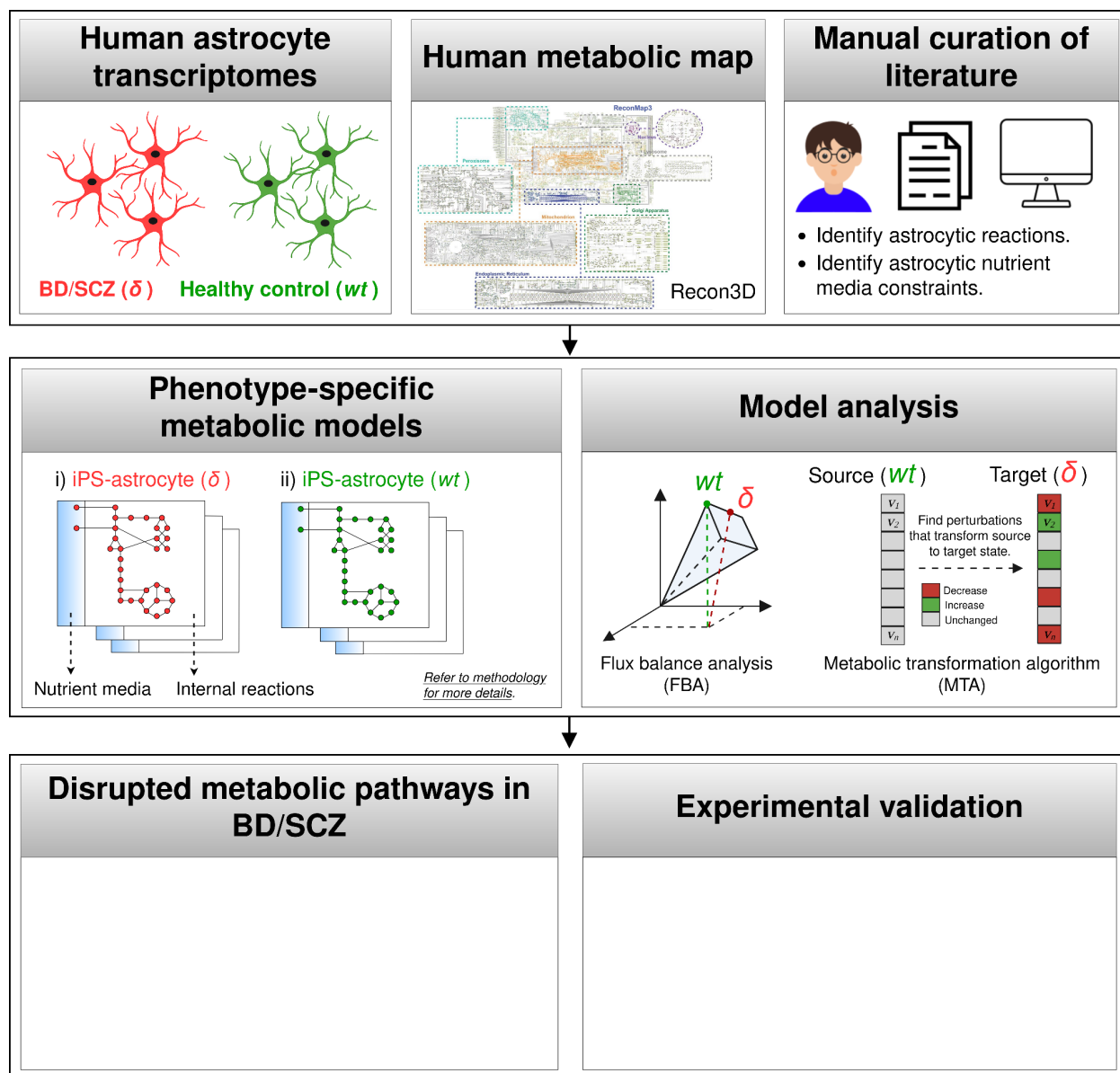Metabolic modeling of astrocytes reveals regulators of lithium response in bipolar disorder.

SUMMARY [TBD]

Graphical abstract

1. Introduction

Bipolar disorder (BD) is a severe psychiatric illness characterized by manic/depressive episodes and persistent neurocognitive impairments [1], affecting 0.5% of the population (ca. 7 million in India) [2]. It is a significant cause of disability, morbidity, and mortality (15% die by suicide) [3]. Lithium (Li+), a WHO "essential medicine", is the most effective drug for BD, reduces suicide risk [4,5] and improves cognition [6]. There are many biochemical pathways which have been implicated in the pathobiology of BD and the mechanisms of Li+, including the inositol metabolism, cyclic nucleotide metabolism, glycogen synthase kinase 3β signaling, glutamate pathways, and circadian clock systems [7]. However, the exact mechanisms are enigmatic leading to absence of predictive markers.

Astrocyte dysfunction has been implicated in BD [8,9] and also in the mechanism of action of Li+ [10,11]. Stable isotope-resolved metabolomics (SIRM) approach showed that Li+ enhanced glycolytic and Krebs cycle activity in both astrocytes and neurons, especially the anaplerotic pyruvate carboxylation (PC). The study also showed that Li+ stimulated the extracellular release of 13C labeled -lactate, -alanine (Ala), -citrate, and -glutamine (Gln), specifically by astrocytes [10]. It has also been shown that concentration of myo-inositol is higher in astrocytes than in neurons, and has been widely considered an astroglial metabolic marker [12]. In addition, cortical neuron cultures do not express the enzyme myo-inositol phosphate synthase (MIP-synthase), but rather depend on extracellular supply of myo-inositol [13]. Overall, these observations make astrocytes more attractive and a probable candidate for Li+ action leading to myo-inositol homeostasis in the brain, compared to neurons.

Because screening for these metabolic pathways in astrocytes, in-vivo or in-vitro, is a substantial task, we adopted an alternative, computational approach to narrow down towards putative candidates that could be experimentally validated. First, by integrating publicly-available transcriptomics data with the constraint-based reconstruction and analysis (COBRA) framework, we have built genome-scale metabolic models (GSMM) of astrocytes derived from BD patients and healthy controls. We improved upon prior brain metabolic models by extensive manual curation of literature to identify the metabolic functions and extracellular nutrient uptake constraints relevant to astrocytes. And subsequently, by using diverse analytical methods we have identified metabolic fluxes that are specifically disrupted in BD patients' astrocytes. One of the advantages of GSMM is that it can describe the metabolic state of cells at a steady state without the need for detailed knowledge of enzymatic kinetics, which is difficult to estimate at a network level. Modeling studies like this have been extensively used in the past decade to explain not only the human metabolism in general [14] but also the effects of human disease phenotypes [15–17].

Our analysis identified biochemical pathways (n=8) that were specifically disrupted in the metabolic models of BD patients who were non-responsive to Li+ treatment. This also included the slower inositol cycle in Li+ non-responder astrocytes, which was in-keeping with the long-standing inositol depletion hypothesis of Li+ in mediating the treatment response in BD [18,19]. [WIP - IDENTIFYING LINKS BETWEEN INOSITOL & REMAINING SEVEN PATHWAYS].

2. Methodology

2.1. Key resources table

REAGENT or RESOURCE	REFERENCE	IDENTIFIER or LINK
Data		
Zhang, Human Primary Astrocyte, RNA-Seq	[20]	GSE73721
Vadodaria, Human iPSC Astrocyte, BD/Ctrl, RNA-Seq	[9]	GSE157509
Koskuvi, Human iPSC Astrocyte, SCZ/Ctrl, RNA-Seq	[21]	GSE191248
Human glia, Proteomics (semi-quantitative immuno-histochemistry abundance)	[22]	https://www.proteinatlas.org/download/normal_tissue.tsv.zip
Recon3D	[14]	https://www.vmh.life/#downloadview
Software and Algorithms		
FastQC	-	https://www.bioinformatics.babraham.ac.uk/projects/fastqc/
Cutadapt	-	https://cutadapt.readthedocs.io/en/stable/
HISAT2	[23]	http://daehwankimlab.github.io/hisat2/

Samtools	[24]	http://samtools.sourceforge.net/
Cufflinks	[25]	http://cole-trapnell-lab.github.io/cufflinks/
org.Hs.eg.db	-	https://bioconductor.org/packages/release/data/annotation/html/org.Hs.eg.db.html
COBRA Toolbox v3.0	[26]	https://opencobra.github.io/cobratoolbox/stable/
iMAT	[27]	-
GIMME	[28]	-
MBA	[29]	-
FastCore	[30]	-
Metabolic Transformation Algorithm (MTA)	[15,31,32]	https://github.com/ImNotaGit/MTA
Gurobi optimizer	-	https://www.gurobi.com/
MATLAB R2015b	-	https://in.mathworks.com/products/matlab.html
R version 3.6.3	-	https://www.r-project.org/
Custom scripts for model generation and analysis	This study	https://github.com/anin90/AstroModel

2.2. Dataset overview

Three previously published transcriptome datasets: "Zhang" [20], "Vadodaria" [9], "Koskuvi" [21], were utilized. In Zhang, the astrocytes were purified from mice, human fetal, and adult brain tissues using immunopanning. The mice data were excluded from our analysis leaving us with 41 human subjects including six fetal astrocyte samples, 12 adult astrocyte samples, eight glioblastoma multiforme (GBM) or sclerotic hippocampal samples, four whole human cortex samples, and 11 human samples of other purified CNS cell types. Healthy astrocytes, except for the GBM and sclerotic samples, were obtained from fetal brain tissue from elective pregnancy terminations at 17–20 gestational weeks or healthy

temporal lobe cortices from patients undergoing neurological surgeries. In Vadodaria, the astrocytes were derived from induced pluripotent stem (iPS) cells generated from fibroblasts of BD patients (n=5), which includes both Li+ responders (n=3) and non-responders (n=2), as well as healthy controls (n=4). The astrocytes were differentiated for five weeks, and subsequently stimulated with 10 ng/mL IL-1b or phosphate buffered saline (PBS) for 5h, followed by RNA-Seq. Similarly, in Koskuvi, the astrocytes were derived from iPS cells generated from fibroblasts of monozygotic twin pairs discordant for SCZ (n=4), which includes both healthy twins (HT, n=4) and SCZ twins (ST, n=4), as well as age- and sex- matched healthy controls (n=6). RNA was extracted from the monolayer culture of iPS-derived astrocytes (150 DIV i.e., days in vitro), followed by RNA-Seq. All three datasets were uniformly processed using a consensus set of tools. After processing and quality control, "Zhang" was used to build metabolic models of primary astrocytes, while "Vadodaria" and "Koskuvi" were used to build metabolic models of iPS-astrocytes.

2.3. Pre-processing and quality control of public data

2.3.1. RNA-sequencing (Zhang, Vadodaria, Koskuvi)

Transcriptome data (FastQ) were obtained by downloading from public repositories (Zhang/Vadodaria/Koskuvi). The non-human samples, if any, were removed from Zhang, Vadodaria and Koskuvi. FastQC (http://www.bioinformatics.babraham.ac.uk/projects/fastqc) was used to assess the quality of the reads and Cutadapt (https://cutadapt.readthedocs.io/en/stable/) was used to remove adapter contamination. HISAT2 [23] was used to align the filtered reads to the human reference genome (GRCh37). Samtools [24] was used for SAM to BAM conversion and sorting. Cufflinks [25] was used to estimate gene-level expression (FPKM), and gene symbols were annotated for NCBI Entrez IDs using org.Hs.eg.db. The non-specific genes i.e., same gene symbol mapping to multiple Entrez IDs or multiple symbols mapping to the same ID were excluded. For Zhang, Vadodaria and Koskuvi, the genes with FPKM $\geq$ 0.1 in at least 50% of all samples were considered, resulting in 13,423, 14,543 and 16,724 genes respectively [ST.X].

2.3.2. Proteomics

The human cortical glial proteomics data from the human protein atlas (HPA) [22] were utilized to provide further evidence of expression in Zhang, Vadodaria and Koskuvi. The reliability scores ('Enhanced', 'Supported', 'Approved', or 'Uncertain') and the semi-quantitative nature of the immunohistochemistry protein abundance ('High', 'Medium', 'Low') were retained [33] [ST.X].

2.4. Metabolic modeling of astrocytes

2.4.1. Integration of phenotype-specific transcriptomes with Recon3D

Recon3D [14], the latest human metabolic reaction library, was used to extract draft metabolic models. While all the samples in the Zhang, Vadodaria, and Koskuvi datasets were processed (FASTQ to FPKM), only a subset of samples was chosen from each dataset for metabolic modeling. In Zhang, only cortical astrocytes from adult samples (n=12) were included. In the Vadodaria dataset, only PBS treated iPS-astrocytes from BD patients (n=5) and healthy controls (n=4) were considered. However, in the Koskuvi dataset, the entire dataset, including iPS-astrocytes from SCZ twin pairs (n=4) and healthy controls (n=6), was utilized for modeling. In Vadodaria, the BD patient data was further divided into Li+ responders (n=3) and non-responders (n=2) for modeling treatment responsiveness. In Koskuvi, the monozygotic twin pairs were further divided into SCZ twins (n=4) and healthy twins (n=4) for modeling the effects of familial/genetic risk. Genes that were detected in the transcriptome (n=13,423, Zhang; n=14,543, Vadodaria; n=16,724, Koskuvi) but had 'uncertain' reliability in the HPA glial proteome were excluded, resulting in a subset of genes that were "transcriptome & proteome" evident (n=4,105, Zhang; n=4,040, Vadodaria; n=4,203, Koskuvi). Metabolic models for eight distinct phenotypes were obtained by constraining Recon3D with the transcriptome data of:

1. Zhang: Primary astrocytes (Primary-Ctrl),
2. Vadodaria: iPS-astrocytes from healthy controls (iPS-Ctrl-i),
3. Vadodaria: iPS-astrocytes from BD patients (iPS-BD),
4. Vadodaria: iPS-astrocytes from BD patients - responders (iPS-BD-R),
5. Vadodaria: iPS-astrocytes from BD patients - non-responders (iPS-BD-NR),
6. Koskuvi: iPS-astrocytes from healthy controls (iPS-Ctrl-ii),
7. Koskuvi: iPS-astrocytes from monozygotic twin pairs - SCZ twins (iPS-ST),
8. Koskuvi: iPS-astrocytes from monozygotic twin pairs - Healthy twins (iPS-HT).

The genes were mapped to reactions using the function *mapExpressionToReactions* in COBRA Toolbox. The reactions were associated with a core reaction set (n=1843, Zhang; n=1765, Vadodaria; n=1836, Koskuvi). Different variants of the model extraction methods (MEMs) such as iMAT [27], GIMME [28], MBA [29] and FastCore [30] were considered. Both absolute (abs) and normalized (norm) FPKM values were used to generate the metabolic models.

a.) $FPKM_{abs}$: A user-defined FPKM value of 2 was chosen as a threshold to define the 'high-confidence' reactions and while those ranging between 0.1 & 2 were used to define the 'medium-confidence' reactions, unless manual curation of the literature dictated otherwise.

b.) $FPKM_{norm.t1}$: The FPKM data matrices were $log10(x + 1)$ transformed and then quantile normalized to obtain $FPKM_{norm}$. The maximum $FPKM_{norm}$ of each gene (g_i) across all samples i.e., $max(g_i)$ was considered. The genes with $max(g_i) > 50th\ percentile$ of the normalized expression vector $max(g_1),\ max(g_2),\ .....,\ max(g_i)$ were chosen as a threshold to define the 'high-confidence' reactions and while those ranging *between the* $25th$ & *the* $50th\ percentile$ were used to define the 'medium-confidence' reactions. The genes *below the* $25th\ percentile$ were considered inactive, unless manual curation of the literature dictated otherwise.

c.) $FPKM_{norm.t2}$: While the normalization is similar to $FPKM_{norm.t1}$, the thresholding is different i.e., $max(g_i) > 25th\ percentile$ and those *between the* $10th$ & $25th\ percentile$ define the 'high-confidence' and 'medium-confidence' reactions respectively, unless manual curation of the literature dictated otherwise.

Draft metabolic models of astrocytes (n=56) were generated from the transcriptomes of eight phenotypes (Primary-Ctrl, iPS-Ctrl-i, iPS-BD, iPS-BD-R, iPS-BD-NR, iPS-Ctrl-ii, iPS-ST and iPS-HT) using four MEMs (iMAT, GIMME, MBA, and FastCore) across three gene expression scales ($FPKM_{abs}$, $FPKM_{norm.t1}$, $FPKM_{norm.t2}$). iMAT and MBA require a 'medium-confidence' threshold to be defined by users, while GIMME and FastCore do not. The MEMs maximize the number of high-confidence and minimize the number of medium-confidence reactions in their output models. Of the 56, the models that captured the least fluxInconsistent reactions, the highest number of core reactions, and the highest overlap with astrocytic reactions (n=649) from Lewis et al. 2010, for each of the eight phenotypes, were chosen for further expansion [ST.X].

2.4.2. Expansion of draft models through manual curation of literature

Extensive manual curation of literature was performed to provide experimental evidence for a subset of reactions (n=159) and their rationale for inclusion and PMIDs that support and refute their activity in astrocytes [ST.X]. As part of this effort, an additional extracellular compartment 'synapse' [s], along with exchange (n=15) and transport reactions (n=14), were included in the 'Primary-Ctrl' model to capture astrocyte-synapse metabolic crosstalk. However, the synaptic compartment and corresponding reactions were not included in the iPS-astrocyte models.

2.4.3. Imposing experimental nutrient uptake constraints

It was assumed that in vivo, all the constituents of ASM would cross the BBB and be available for uptake by astrocytes. Hence, the 'Primary-Ctrl' model's extracellular compartment [e] was constrained by all metabolites and ions that i) constitute the astrocyte sustenance medium (ASM) [34], and ii) cross the blood brain barrier (BBB) [35]. The remaining four iPS-astrocyte models' extracellular [e] compartments were constrained by ASM alone, representing culture media conditions. The metabolic components of the ASM, which consists of Neurobasal medium, Minimum Essential Medium - Non-Essential Amino Acids Solution, GlutaMAX Supplement, and N-2 Supplement, were obtained from the Thermo Fisher Scientific™ website. The metabolic components of the BBB were obtained from Thiele et al., 2020. There are 22 components that overlap between the ASM (n=44) and BBB (n=45). To simulate nutrient uptake, all nutrient uptakes in the model except for the 67 exchanges added to the extracellular compartment [e], for which uptake rates were set to -10mmol/gDw/h, were set to 0 [ST.X].

2.5. Identifying disrupted reactions & subSystems in BD metabolic models.

2.5.1. Flux balance analysis (FBA)

A metabolic network consisting of m metabolites and n reactions is represented by a stoichiometric matrix S where S_{ij} represents the stoichiometric coefficient of metabolite i in reaction j. The flux vector for each reaction in the network is represented by v. Flux balance analysis (FBA) assumes a steady-state mass balance wherein the sum of the input flux equals the sum of the output flux. This follows as, $dx_i / dt = 0$ i.e. the change in concentration of the ith metabolite over time is zero [36]. Flux variability analysis (FVA) was used to calculate the minimum and maximum flux through each reaction in all five metabolic models subject to constraints,

$$min/max \; c^t \, x, \; s.t. \quad s.v = dx/dt = 0 \, , \qquad\qquad (1)$$

$$v_{min} \leq v_j \leq v_{max} \, , \qquad\qquad (2)$$

where the equation (1) corresponds to the steady-state mass-balance constraints, whereas equation (2) corresponds to the reaction directionality and capacity constraints. The ratio of flux span (FSr) [37] for each reaction was calculated as follows,

$$FSr \; (healthy \; vs \; disease) \; = \; \frac{abs(FVAmax_{j,healthy} - FVAmin_{j,healthy})}{abs(FVAmax_{j,disease} - FVAmin_{j,disease})} \, , \qquad\qquad (3)$$

where $FVAmax$ and $FVAmin$ are the maximum and minimal flux through the jth reaction in the model. FSr can be calculated only for those reactions that are captured by both the models under comparison. The reactions with $FSr > 1.5\ and < 0.8$ were identified for each phenotype-of-interest (n=4 i.e., BD; BD_Responder; BD_NonResponder; SCZ-Twin), and subsequently considered for downstream analysis [ST.X].

2.5.2. Metabolic transformation algorithm (MTA)

The metabolic transformation algorithm (MTA) [15,31,32] identifies reactions in a metabolic network whose inhibition facilitates a transformation between two metabolic states (e.g., from diseased to healthy states, or vice-versa). The inputs to MTA are i) the transcriptomic measurements of the source and target states, and ii) the reference metabolic model. For each transformation analysis, MTA follows a two-step process: i) determining the flux distribution of the source metabolic state (v^{ref}) using iMAT followed by ACHR sampling of the solution space. ii) determining the set of genes whose expression has significantly elevated or reduced between the source and target states. Using i) and ii), MTA computes a transformation score for each of the metabolic reactions in the cell, and usually, the 10-20% reactions with the highest MTA score contain promising candidate targets. For each phenotype-of-interest, we ran MTA twice, by swapping the source and the target states. E.g., in order to identify the reactions relevant to BD, we identified the reactions that transformed i) "iPS-Ctrl" to "iPS-BD", and ii) "iPS-BD" to "iPS-Ctrl". For either runs, the top 20% predictions were first identified, and subsequently their union sets were considered for downstream analysis [ST.X].

2.5.3. Filtering reactions relevant to phenotype-of-interest.

From the reactions as identified by FVA ($FSr > 1.5\ and < 0.8$) or MTA (top 20%), filters were applied to select for reactions that were relevant to the phenotype-of-interest. While defining the filters, it was important to consider the fact that the treatment responders and the non-responders together comprise the BD cohort. Hence the fluxes relevant to "BD_R" and "BD_NR'' can share overlaps with "BD".

Phenotype-of-interest	Filtering criteria
BD [1]	Specifically disrupted in "iPS-Ctrl vs iPS-BD" & unchanged between control models.
BD-Responder [2]	Specifically disrupted in "iPS-Ctrl vs iPS-BD-Responder" & unchanged between control models.
BD-NonResponder [3]	Specifically disrupted in "iPS-Ctrl vs iPS-BD-NonResponder" & unchanged between control models.
SCZ-Twin [4]	Specifically disrupted in "iPS-Ctrl vs iPS-SCZ-Twin" &

	unchanged between control models.

[1] Can share overlaps with BD-Responder, BD-NonResponder and SCZ-Twin.
[2] Can share overlaps with BD and SCZ-Twin but not with BD-NonResponder.
[3] Can share overlaps with BD and SCZ-Twin but not with BD-Responder.
[4] Can share overlaps with BD, BD-Responder and BD-NonResponder.

Table.1. Reaction filtering criteria. "Unchanged between control models" means the reactions that were not found to be disrupted in "iPS-Ctrl vs Primary-Ctrl".

2.5.4. Reaction-set enrichment analysis (RSEA).

To test for overrepresentation of metabolic subSystems, the reactions as identified from the above steps were tested against the Recon3D reaction annotations, using hypergeometric tests (phyper function in R), followed by multiple testing correction (Benjamini–Hochberg). The subSystems with $P_{FDR} < 0.05$ were considered significant. The set of background reactions (i.e., the reactions against which the set of filtered reactions were tested) were all reactions present in the metabolic model, minus the reactions present in the subSystem being tested.

2.5.5. Identifying disruptions that are significant across modules.

Here, a 'module' was defined as the list of subSystems that were predicted to be significant by RSEA, using either of the analytical approaches i.e., FBA/MTA. E.g. 'FVA_BD_NR_norm_t1' is a module - where 'FVA' is the analytical method, 'BD_NR' is the phenotype-of-interest and 'norm_t1' is the gene expression thresholding of the metabolic model. For each phenotype-of-interest (BD, BD-Responder, BD-NonResponder and SCZ-Twin), we generated six modules (i.e., derived using three expression thresholds and two analytical methods), and identified the subSystems that were disrupted in at least two or more modules [ST.X].

2.6. Data, figures and code availability.

This study did not generate experimental data. Raw transcriptome data used in this study were publicly available. Most figure panels were generated programmatically in R with the exception of Fig.X which was created using BioRender.com (full license) and Diagrams.net (open source). All original code has been deposited at GitHub and is publicly available. References, identifiers and the link to the GitHub repository are provided in the key resources table.

3. Results

3.1. Building and testing astrocyte metabolic models. (Figure.1)

Draft metabolic models of astrocytes (n=56) were extracted for eight distinct phenotypes, including BD patients (iPS-BD, iPS-BD-R, iPS-BD-NR), SCZ twin (iPS-ST), healthy twin (iPS-HT) and healthy controls (Primary-Ctrl, iPS-Ctrl-i, iPS-Ctrl-ii), by using transcriptome data and glial proteomics data as a constraint on the Recon3D human metabolic knowledgebase. The gene expression threshold determines the model contents, and there's no one model that's poised to explain the underlying biology [38]. Hence, three metabolic models were built for each of the eight phenotypes by using different FPKM thresholds. Of the 56 models, only the iMAT-derived models (n=24) satisfied our selection criteria and only those were further expanded (refer Methodology section 2.4. for more details) [ST.X]. First, the properties of the 24 models, before (preExpansion) and after expansion (postExpansion), were evaluated (**Fig.1.a-e**). The final models (i.e., postExpansion) consisted of 5,342–6,305 reactions and 3,679–4,273 metabolites. The flux inconsistency, which refers to the blocked reactions, ranged between ~22-29% in the final models, which is primarily driven by the nutrient media constraints, as opposed to zero blocked reactions in the draft models due to the unconstrained nutrient media. This constraint was necessary to ensure that the final models operated solely on physiologically relevant nutrient media conditions. The core reactions captured by all models ranged between ~70-98%, and the Lewis et al. astrocytic reactions captured by all models ranged between ~40-53%. The literature curated reactions (n=159) were also used as "metabolic tasks", and all 24 models passed ~90-93% of the tasks. A comparison was performed between our models (This Study, n=24) and previously published mass-action models of brain metabolism (Predecessor, n=11) (**Fig.1.f-g**). The growth in the size of the models over time is mainly due to the ongoing development of larger metabolic knowledge bases like Recon3D. Overall, the statistics indicated that our models do recapitulate astrocyte physiology; were in-par with its equivalents [16] and were ready to be deployed for downstream analysis. However, our literature curation efforts failed to identify and test for the negative functions of astrocytes which could potentially lead to false positive and false negative predictions by our models. We have provided the comprehensive details of all 24 models on Github for open access for the scientific community.
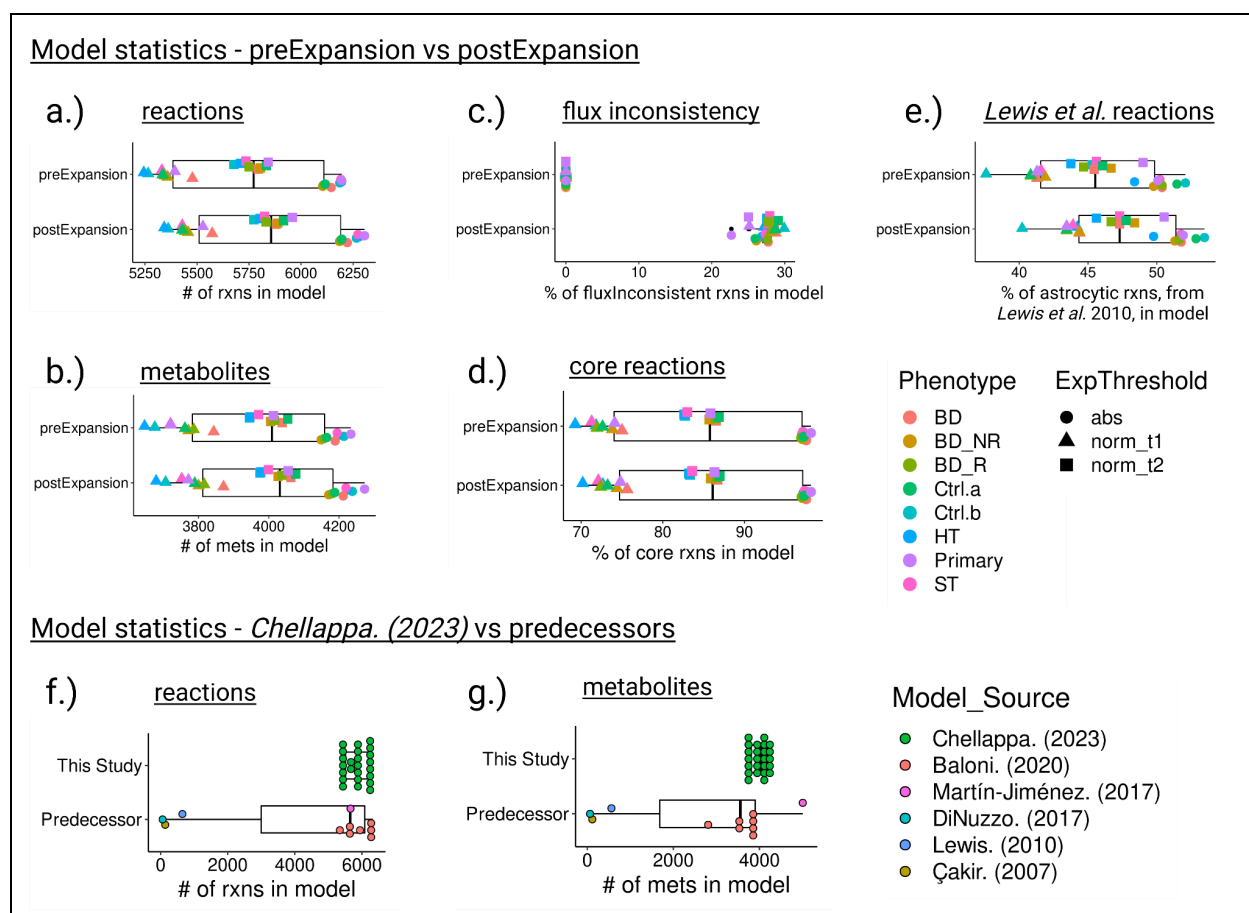
Figure.1: **Model statistics**. **(a-e)** Differences in model statistics observed between the iMAT-derived draft models (preExpansion, n=24) and the final models (postExpansion, n=24) of astrocyte metabolism, that were generated for five phenotypes across three gene expression thresholds. The model statistics include the # of reactions, # of metabolites, % of flux inconsistent reactions, % of core reactions and % of astrocytic reactions (Lewis et al. 2010), captured in the respective models. **(f-g)** Differences in model statistics observed between the models that were built as a part of this study (This Study, n=24) and those captured by previous studies (Predecessor, n=11). Due to the unavailability of the reconstructions for most of the predecessors, with the exception of Lewis et al. (2010) and Baloni et al. (2020), only the # of reactions and metabolites were compared.

3.2. Metabolic subsystems disrupted in BD and SCZ patients' astrocytes (Figure.2.a)

To identify fluxes that are disrupted in our phenotypes-of-interest (BD, BD-Responder, BD-NonResponder and SCZ-Twin), the models (n=24) were first divided into groups based on their FPKM thresholds (n=3). This resulted in five models within each group. The flux distributions of the models within each group were analyzed using two methods - FVA and MTA. Filters were applied to select for reactions that were relevant to each

phenotype-of-interest, followed by reaction set enrichment analysis (RSEA). The metabolic subsystems that were disrupted ($P_{FDR} < 0.05$) in at least two or more modules were identified (Refer to the Methodology section 2.5. for more details). Thirteen subsystems were predicted to be disrupted by at least two or more modules across either of the four phenotypes-of-interest (**Fig.2.a**). However, none of these disruptions were found to be significant across all six modules while considering the $mean(P_{FDR}) < 0.05$. Of the 13 disrupted subsystems, fatty acid oxidation (FAO) was the only one that was found to be disrupted across the two psychiatric disorders i.e., BD (four modules) and SCZ (three modules). In both BD and SCZ, disruptions in FAO were observed in both mitochondria and peroxisomes, indicating alterations in medium chain, long chain, and very-long chain fatty acids [ST.X]. The involvement of fatty acid oxidation (FAO) in psychotic disorders is supported by sparse and inconsistent evidence [39]. The inconsistencies observed in these studies can be attributed to confounding factors such as medication usage, lifestyle, etc. Moreover, many of these studies investigated fatty acid alterations in peripheral samples like erythrocyte membranes, which may not necessarily corroborate findings from post-mortem brains or iPS-cells obtained from psychiatrically ill patients. However, a recent study revealed that the brain critically depends on the astrocytic oxidative phosphorylation (OxPhos) to break down fatty acids (FAs) and maintain lipid balance. Disrupted astrocytic OxPhos leads to the accumulation of lipid droplets (LD) and subsequent neurodegeneration, resembling key aspects of Alzheimer's disease (AD) [40], which shares clinical symptoms and biological processes with BD and SCZ. However, the disruptions in OxPhos fluxes were not predicted by our models, likely due to degeneracy in metabolic networks [41].
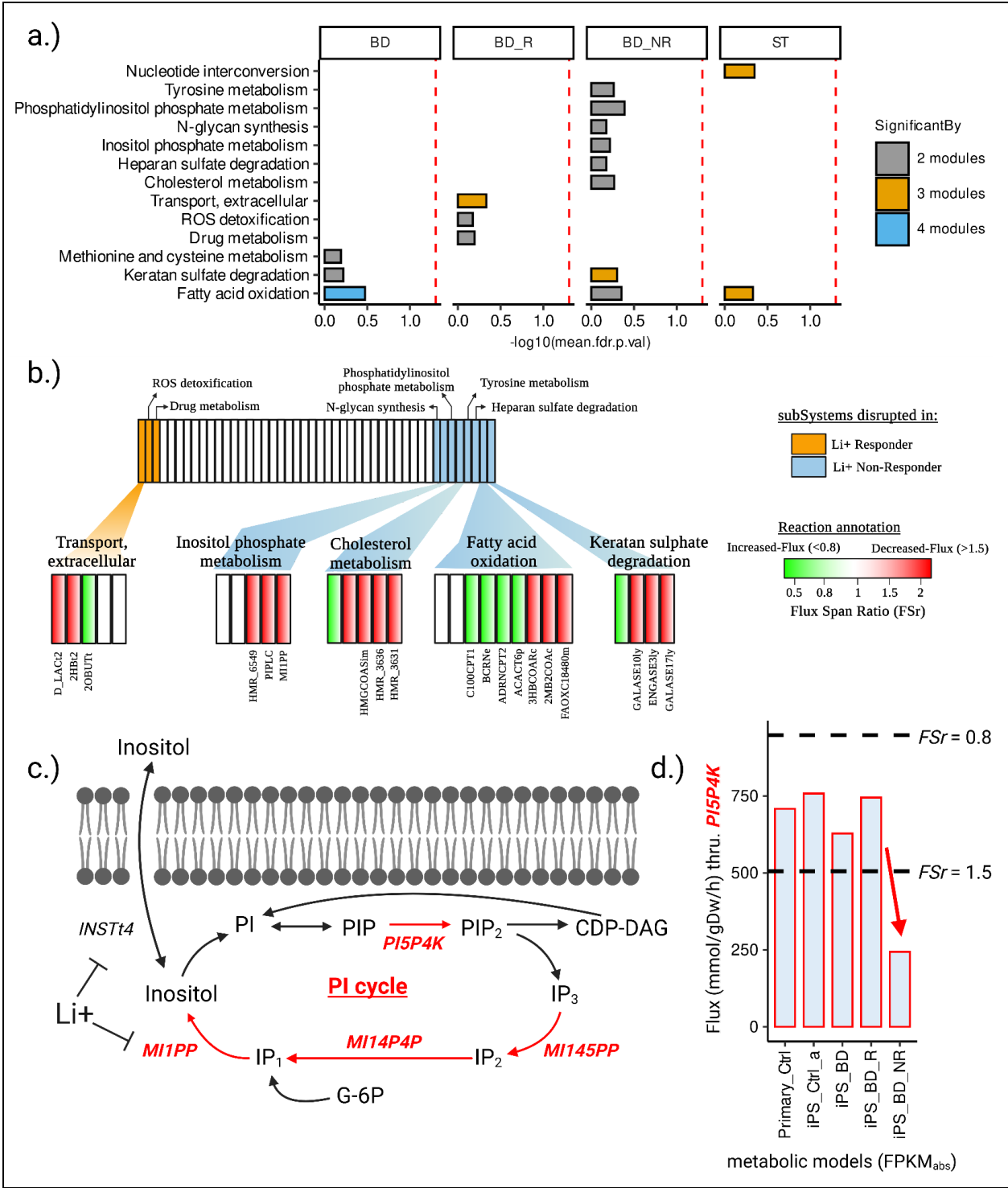
Figure.2: **Metabolic subsystems disrupted in BD and SCZ patients' astrocytes**. **(a)** Metabolic subSystems (n=13) predicted to be disrupted by at least two or more modules across either of the four phenotypes-of-interest (BD, BD-Responder, BD-NonResponder and SCZ-Twin). **(b)** Metabolic subSystems (top) and reactions (bottom) predicted to be disrupted by at least two or more modules in Li+ responders (n=3) and non-responders

(n=8). **(c)** Metabolic fluxes (n=4) through the inositol phosphate metabolism cycle were found to be reduced (red) specifically in Li+ non-responder metabolic models. **(d)** Bar-plot highlighting the reduction of flux through Phosphatidylinositol-5-Phosphate 4-Kinase (PI5P4K) specifically in Li+ non-responder metabolic model.

3.3. Slower inositol cycle in Li+ non-responder astrocytes. (Figure.2b-d)

Eight subsystems were predicted to be specifically disrupted in the Li+ non-responders models, while three subsystems were specifically disrupted in the Li+ responders models. There were no subsystems disrupted across both Li+ responders and non-responders (**Fig.2.b**). Among the disrupted subsystems in non-responders, inositol phosphate (IP) metabolism was identified. The flux through the reactions in this pathway (n=4) was reduced, indicating slower synthesis rates compared to the Li+ responder and the control models (**Fig.2.c-d**). The myo-inositol 1-phosphate phosphatase (MI1PP), one of the four disrupted reactions in the IP metabolism, has a long-standing association with Li+'s mechanisms of action [18]. The "inositol depletion" hypothesis posits that the depletion of inositol by Li+ reduces the brain excitability in BD [18]. And this may happen through the ability of Li+ to,

1. Inhibit MI1PP (IMAPase) activity [18],
2. Inhibit plasma membrane inositol transporters [42],
3. Regulate the rate of inositol synthesis [19].

Regardless of the molecular mechanism of Li+ action, in BD patients inositol concentrations can change, and may be further altered by Li+ treatment [43]. In contrast to the majority of metabolism studies that focus on metabolite concentrations, our model predictions are exclusively on fluxes, which represent the rates of reactions, and alterations in flux levels do not always indicate changes in metabolite concentrations [44]. And metabolite concentrations in a cell can increase due to fast synthesis or slower degradation processes. As a result, two interpretations can be derived from our model prediction of slow inositol synthesis rates specifically in Li+ non-responders:

1. Our models challenge the depletion hypothesis, which suggests that faster synthesis of inositol is expected due to its potential accumulation. This implies that there may be other factors contributing to the slower flux observed in Li+ non-responders.

2. Alternatively, the slower flux could be indicative of lower enzyme concentrations that hinder the actions of Li+ and subsequently impact the responsiveness in BD patients. It is important to note that this slower flux is only observed in the models of Li+ non-responders, while in Li+ responders, the inositol fluxes remain

unaffected. This might suggest that the levels of inositol monophosphatase (IMPAse) may be maintained at a higher level in Li+ responders, facilitating the desired response.

While the latter explanation appears to be the most plausible and parsimonious based on our predictions, experimental validation is necessary to confirm these hypotheses. Our models successfully capture the disruption of inositol fluxes, a well-known aspect of lithium biology. This validation enhances trust in the model predictions, and justifies further investigation of the novel predictions, such as the involvement of remaining seven disrupted subsystems in Li+ non-responders that may not have been previously reported in the literature regarding BD/Li+ biology.

3.4. Identifying links between inositol and remaining disrupted subSystems.
(-------- WIP ------------)

3.5. Experimental validation of model predictions.
(-------- YET TO BE PLANNED------------)

4. Discussions

REFERENCES
1. Grande, I., Berk, M., Birmaher, B. & Vieta, E. Bipolar disorder. *The Lancet* **387**, 1561–1572 (2016).

2. Murray, C. J. L. & Lopez, A. D. Measuring global health: motivation and evolution of the Global Burden of Disease Study. *The Lancet* **390**, 1460–1464 (2017).

3. Miller, J. N. & Black, D. W. Bipolar Disorder and Suicide: a Review. *Curr. Psychiatry Rep.* **22**, 6 (2020).

4. Chen, P. *et al.* Mood stabilizers and risk of all‑cause, natural, and suicide mortality in bipolar disorder: A nationwide cohort study. *Acta Psychiatr. Scand.* **147**, 234–247 (2023).

5. Tondo, L. *et al.* Clinical use of lithium salts: guide for users and prescribers. *Int. J. Bipolar Disord.* **7**, (2019).

6. Burdick, K. E. *et al.* The association between lithium use and neurocognitive performance in patients with bipolar disorder. *Neuropsychopharmacology* **45**, 1743–1749 (2020).

7. Dudev, T., Mazmanian, K., Weng, W. H., Grauffel, C. & Lim, C. Free and Bound Therapeutic Lithium in Brain Signaling. *Acc. Chem. Res.* **52**, 2960–2970 (2019).

8. Santos, R. *et al.* Differentiation of Inflammation-Responsive Astrocytes from Glial Progenitors Generated from Human Induced Pluripotent Stem Cells. *Stem Cell Rep.* **8**, 1757–1769 (2017).

9. Vadodaria, K. C. *et al.* Altered Neuronal Support and Inflammatory Response in Bipolar Disorder Patient-Derived Astrocytes. *Stem Cell Rep.* **16**, 825–835 (2021).

10. Fan, T. W. M. *et al.* Stable isotope-resolved metabolomic analysis of lithium effects on glial-neuronal metabolism and interactions. *Metabolomics* **6**, 165–179 (2010).

11. Rivera, A. D. & Butt, A. M. Astrocytes are direct cellular targets of lithium treatment: novel roles for lysyl oxidase and peroxisome-proliferator activated receptor-γ as astroglial targets of lithium. *Transl. Psychiatry* **9**, 211 (2019).

12. Harris, J. L., Choi, I. Y. & Brooks, W. M. Probing astrocyte metabolism in vivo: Proton magnetic resonance spectroscopy in the injured and aging brain. *Front. Aging Neurosci.* **7**, 1–8 (2015).

13. Daniel, E. D., Cheng, L., Maycox, P. R. & Mudge, A. W. The common inositol-reversible effect of mood stabilizers on neurons does not involve GSK3 inhibition, myo-inositol-1-phosphate synthase or the sodium-dependent myo-inositol transporters. *Mol. Cell. Neurosci.* **32**, 27–36 (2006).

14. Brunk, E. *et al.* Recon3D enables a three-dimensional view of gene variation in human metabolism. *Nat. Biotechnol.* **36**, 272–281 (2018).

15. Auslander, N. *et al.* An integrated computational and experimental study uncovers FUT9 as a metabolic driver of colorectal cancer. *Mol. Syst. Biol.* **13**, 956 (2017).

16. Baloni, P. *et al.* Metabolic Network Analysis Reveals Altered Bile Acid Synthesis and Metabolism in Alzheimer's Disease. *Cell Rep. Med.* **1**, 100138 (2020).

17. Dougherty, B. V. *et al.* Identifying functional metabolic shifts in heart failure with the

integration of omics data and a heart-specific, genome-scale model. *Cell Rep.* **34**, 108836 (2021).

18. Berridge, M. J., Downes, C. P. & Hanley, M. R. Neural and developmental actions of lithium: A unifying hypothesis. *Cell* **59**, 411–419 (1989).

19. Saiardi, A. & Mudge, A. W. Lithium and fluoxetine regulate the rate of phosphoinositide synthesis in neurons: a new view of their mechanisms of action in bipolar disorder. *Transl. Psychiatry* **8**, (2018).

20. Zhang, Y. *et al.* Purification and Characterization of Progenitor and Mature Human Astrocytes Reveals Transcriptional and Functional Differences with Mouse. *Neuron* **89**, 37–53 (2016).

21. Koskuvi, M. *et al.* Contribution of astrocytes to familial risk and clinical manifestation of schizophrenia. *Glia* **70**, 650–660 (2022).

22. Uhlén, M. *et al.* Tissue-based map of the human proteome. *Science* **347**, (2015).

23. Kim, D., Paggi, J. M., Park, C., Bennett, C. & Salzberg, S. L. Graph-based genome alignment and genotyping with HISAT2 and HISAT-genotype. *Nat. Biotechnol.* **37**, 907–915 (2019).

24. Li, H. *et al.* The Sequence Alignment/Map format and SAMtools. *Bioinformatics* **25**, 2078–2079 (2009).

25. Trapnell, C. *et al.* Transcript assembly and quantification by RNA-Seq reveals unannotated transcripts and isoform switching during cell differentiation. *Nat. Biotechnol.* **28**, 511–5 (2010).

26. Heirendt, L. *et al.* Creation and analysis of biochemical constraint-based models using the COBRA Toolbox v.3.0. *Nat. Protoc.* **14**, 639–702 (2019).

27. Zur, H., Ruppin, E. & Shlomi, T. iMAT: an integrative metabolic analysis tool. *Bioinformatics* **26**, 3140–3142 (2010).

28. Becker, S. A. & Palsson, B. O. Context-Specific Metabolic Networks Are Consistent with

Experiments. *PLoS Comput. Biol.* **4**, e1000082 (2008).

29. Jerby, L., Shlomi, T. & Ruppin, E. Computational reconstruction of tissue-specific metabolic models: Application to human liver metabolism. *Mol. Syst. Biol.* **6**, 1–9 (2010).

30. Vlassis, N., Pacheco, M. P. & Sauter, T. Fast Reconstruction of Compact Context-Specific Metabolic Network Models. *PLoS Comput. Biol.* **10**, e1003424 (2014).

31. Cheng, K. *et al.* Genome‑scale metabolic modeling reveals SARS‑CoV‑2‑induced metabolic changes and antiviral targets. *Mol. Syst. Biol.* **17**, (2021).

32. Yizhak, K., Gabay, O., Cohen, H. & Ruppin, E. Model-based identification of drug targets that revert disrupted metabolism and its application to ageing. *Nat. Commun.* **4**, 2632 (2013).

33. Kuo, C.-C., Chiang, A. W. T., Baghdassarian, H. M. & Lewis, N. E. Dysregulation of the secretory pathway connects Alzheimer's disease genetics to aggregate formation. *Cell Syst.* **12**, 873-884.e4 (2021).

34. Zhao, C. *et al.* Mutant C9orf72 human iPSC‑derived astrocytes cause non‑cell autonomous motor neuron pathophysiology. *Glia* **68**, 1046–1064 (2020).

35. Thiele, I. *et al.* Personalized whole‑body models integrate metabolism, physiology, and the gut microbiome. *Mol. Syst. Biol.* **16**, (2020).

36. Orth, J. D., Thiele, I. & Palsson, B. Ø. What is flux balance analysis?,. *Nat Biotechnol* **28**, 245–248 (2011).

37. Sahoo, S. & Thiele, I. Predicting the impact of diet and enzymopathies on human small intestinal epithelial cells. *Hum. Mol. Genet.* **22**, 2705–2722 (2013).

38. Opdam, S. *et al.* A Systematic Evaluation of Methods for Tailoring Genome-Scale Metabolic Models. *Cell Syst.* **4**, 318-329.e6 (2017).

39. Mocking, R. J. T., Assies, J., Ruhé, H. G. & Schene, A. H. Focus on fatty acids in the neurometabolic pathophysiology of psychiatric disorders. *J. Inherit. Metab. Dis.* **41**, 597–611 (2018).

40. Mi, Y. *et al.* Loss of fatty acid degradation by astrocytic mitochondria triggers neuroinflammation and neurodegeneration. *Nat. Metab.* **5**, 445–465 (2023).

41. Edelman, G. M. & Gally, J. A. Degeneracy and complexity in biological systems. *Proc. Natl. Acad. Sci.* **98**, 13763–13768 (2001).

42. Dai, G., Yu, H., Kruse, M., Traynor-Kaplan, A. & Hille, B. Osmoregulatory inositol transporter SMIT1 modulates electrical activity by adjusting $PI(4,5)P_2$ levels. *Proc. Natl. Acad. Sci.* **113**, (2016).

43. Raghu, P., Joseph, A., Krishnan, H., Singh, P. & Saha, S. Phosphoinositides: Regulators of Nervous System Function in Health and Disease. *Front. Mol. Neurosci.* **12**, (2019).

44. Flam, E. & Arany, Z. Metabolite signaling in the heart. *Nat. Cardiovasc. Res.* **2**, 504–516 (2023).